

Designing soft and tough multiple-network elastomers: Impact of reversible radical deactivation on filler network architecture and fracture toughness

Aaliyah Z. Dookhith, Zidan Zhang, Venkat Ganesan and Gabriel E. Sanoja*

McKetta Department of Chemical Engineering, University of Texas at Austin, Austin, TX 78712, USA

Table of Contents

FIGURES AND TABLES	4
<i>Synthesis of mechanophore and calibration molecule</i>	4
Figure S1. ¹ H NMR of mechanophore DAOL in CD ₂ Cl ₂	4
Figure S2. ¹ H NMR of calibration molecule in CD ₂ Cl ₂	4
<i>Synthesis of filler networks</i>	5
Table S1. Synthesis of polymer networks by FRP, RAFT and ATRP.	5
Figure S3. Pre-stretch of filler networks synthesized by free radical, RAFT, and ATRP polymerizations. ..	5
<i>Mechanical properties of multiple networks</i>	6
Figure S4. Stress-stretch curves of filler ($\lambda_0 = 1.0$) and multiple-networks ($\lambda_0 = 1.6$) in single-edge notch fracture tests (T = 23°C and $\dot{\lambda} = 0.003s^{-1}$)	6
Figure S5. Stress-stretch curves of multiple-networks under step-cyclic loads	7
Figure S6. Viscoelastic shift factors of multiple-networks	7
<i>Rate- and temperature-dependent fracture of multiple-networks</i>	8
Figure S7. Stress-stretch curves and crack length from single-edge notch fracture tests conducted in multiple-networks at various temperatures	8
Figure S8. Stress-stretch curves and crack length from single-edge notch fracture tests conducted in multiple-networks at various loading rates	9
Figure S9. Critical stretch for crack propagation in single-edge notch fracture tests of multiple-networks	10
Table S2. Single-edge notch fracture tests in multiple-networks	11
Table S3. Crack propagation velocities, v, in multiple networks with different filler networks	11
<i>Polymer mechanochemistry</i>	12
Table S4. Synthesis of mechanophore-labeled polymer networks by free radical, RAFT and ATRP copolymerization.	12
Figure S10. Mechanical properties of filler networks without (-) and with (+) mechanophore,	13
Figure S11. Mechanical properties of multiple networks made from filler networks without (-) and with (+) mechanophore	14

Figure S12. Calibration of fluorescence intensity	15
Figure S13. Image processing and confocal imaging of fractured specimens.....	16
Figure S14. Representative crack surfaces of multiple networks (i) containing filler networks synthesized by free radical, RAFT and ATRP polymerizations and (ii) fractured at different temperatures	17
Figure S15. Fraction of activated mechanophores in multiple networks (i) containing filler networks synthesized by free radical, RAFT, and ATRP polymerizations and (ii) fractured at different temperatures	18
Figure S16. Representative crack surfaces of multiple networks (i) containing filler networks synthesized by free radical, RAFT and ATRP polymerizations and (ii) fractured at different rates	19
Figure S17. Fraction of activated mechanophores in multiple networks (i) containing filler networks synthesized by free radical, RAFT and ATRP polymerizations and (ii) fractured at different rates	20
Figure S18.....	21
Figure S19. Damage localization in multiple-networks	22
Figure S20. Fracture toughness as function of the reduced crack propagation velocity.....	23
Figure S21. Damage as a function of the reduced crack propagation velocity	23
Figure S22. Scaling behavior of the fracture toughness with respect to the damage zone size.	24
Figure S23. Molecular picture of fracture in multiple-networks	25
Figure S24. Damage increases with the critical stretch within the filler network but depends on the synthesis method.....	26
Figure S25. Toughness increases with the critical stretch within the filler network. However, the synthesis method – FRP, RAFT, and ATRP - plays an important role in energy dissipation	26
Figure S26. Damage increases with the critical stretch within the filler network	27
Figure S27. Energy dissipated per broken filler network chain depends on the polymerization method used to synthesize the filler network.....	27
<i>Optical properties of multiple networks</i>	28
Figure S28. Phase separation in filler networks synthesized by free radical, RAFT and ATRP	28
MODELS AND CALCULATIONS	29
<i>Volume fraction and pre-stretch of the filler networks</i>	29
SIMULATION DETAILS	29
<i>Reactive Monte-Carlo Simulations</i>	29
Table S5. Parameters used to simulate free radical, RAFT and ATRP copolymerizations	30
Figure S29. Chain length distributions in the load-bearing phase of the filler networks synthesized by FRP, RAFT, and ATRP.....	31
<i>Coarse-Grained Molecular Dynamics Simulations</i>	31

Figure S30. Snapshots for the polymer network prepared through ATRP during uniaxial deformation	31
Figure S31. The number density of equilibrated polymer network before deformation	32
Figure S32. The linear regression of the initial part of stress-strain curve for Young's modulus	32
Figure S33. The count (a, c, e) and fraction (b, d, f) of the closest distances between chain scission events	34
Figure S34. Average distance, d, between scission events in polymer networks	35
Figure S35. Potential energy in the networks during deformation	35
REFERENCES	36

FIGURES AND TABLES

Synthesis of mechanophore and calibration molecule

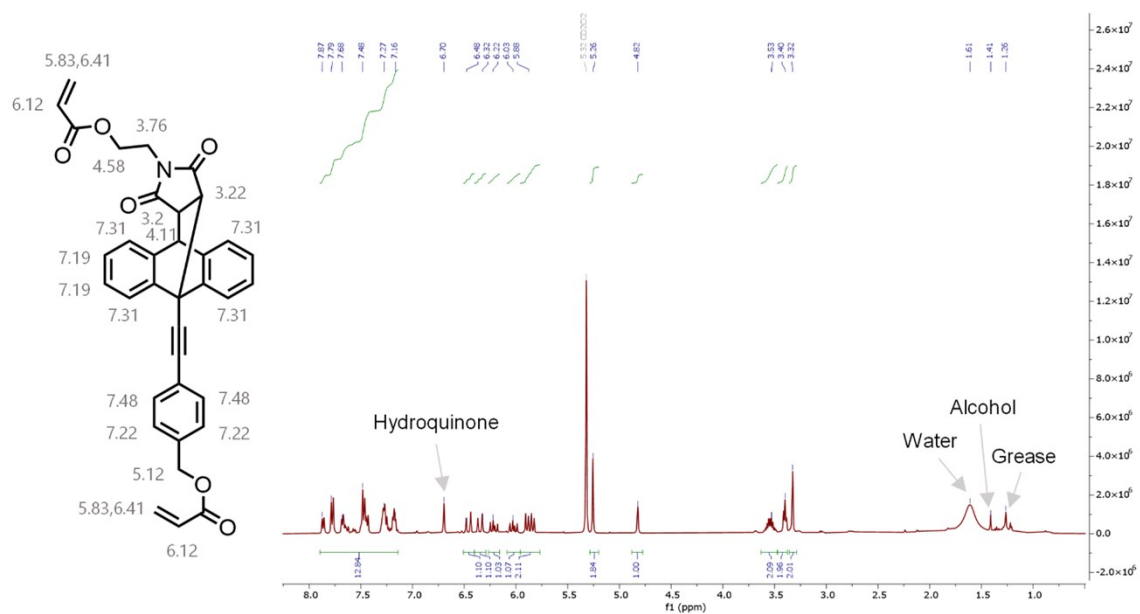


Figure S1. ¹H NMR of mechanophore DAOL in CD₂Cl₂.

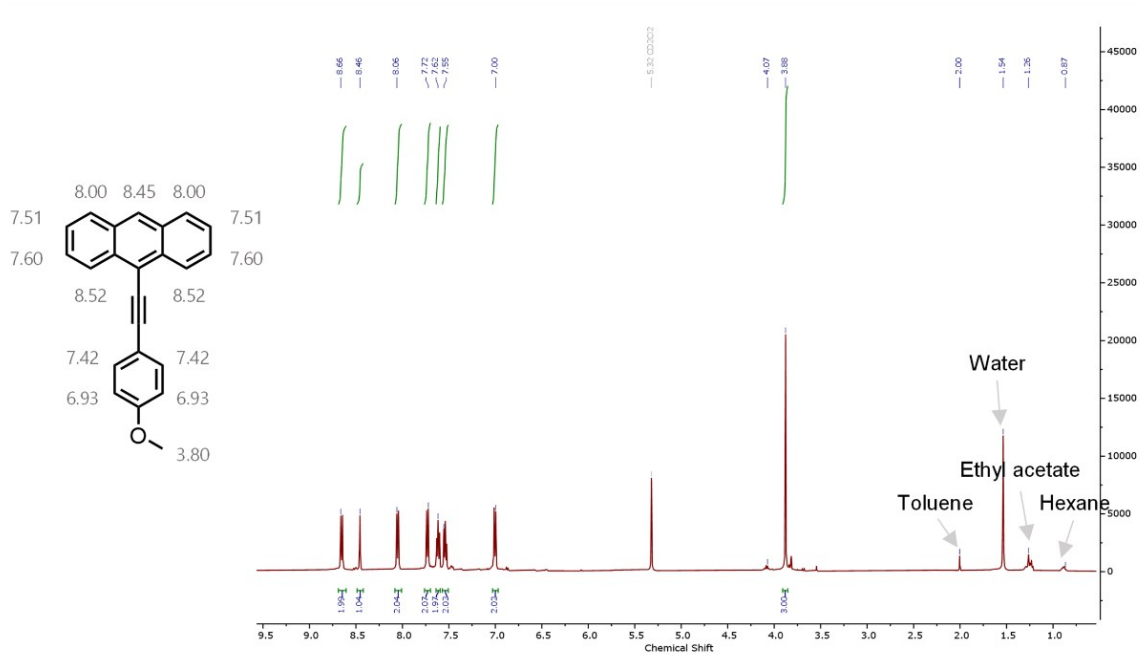


Figure S2. ¹H NMR of calibration molecule in CD₂Cl₂.

Synthesis of filler networks

Table S1. Synthesis of polymer networks by FRP, RAFT and ATRP.

Mechanism	EA			BDA			Initiator (HMP or EBiB)			CTA or Copper	
	x [mol%]	V [mL]	m [g]	x [mol%]	V [mL]	m [g]	x [mol%]	V [mL]	m [g]	x [mol%]	m [g]
FRP	99.4	3	2.8	0.5	0.026	0.03	0.1	0.004	0.005	-	-
RAFT	98.9	3	2.8	1.0	0.053	0.06	0.02	0.001	0.001	0.1	0.009
ATRP	98.9	3	2.8	1.0	0.053	0.06	0.07	0.003	0.004	0.007	0.0003

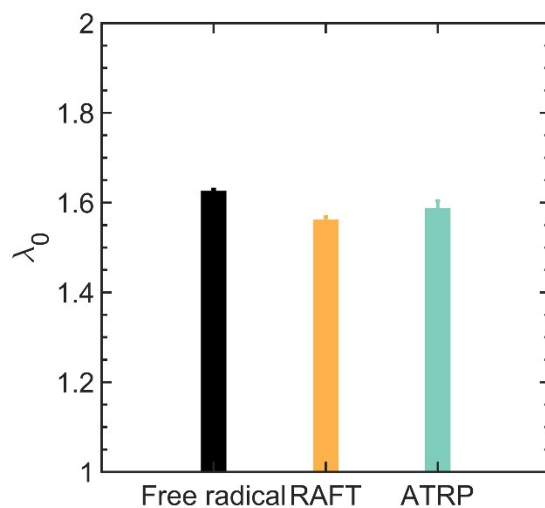


Figure S3. Pre-stretch of filler networks synthesized by free radical, RAFT, and ATRP polymerizations.

Mechanical properties of multiple networks

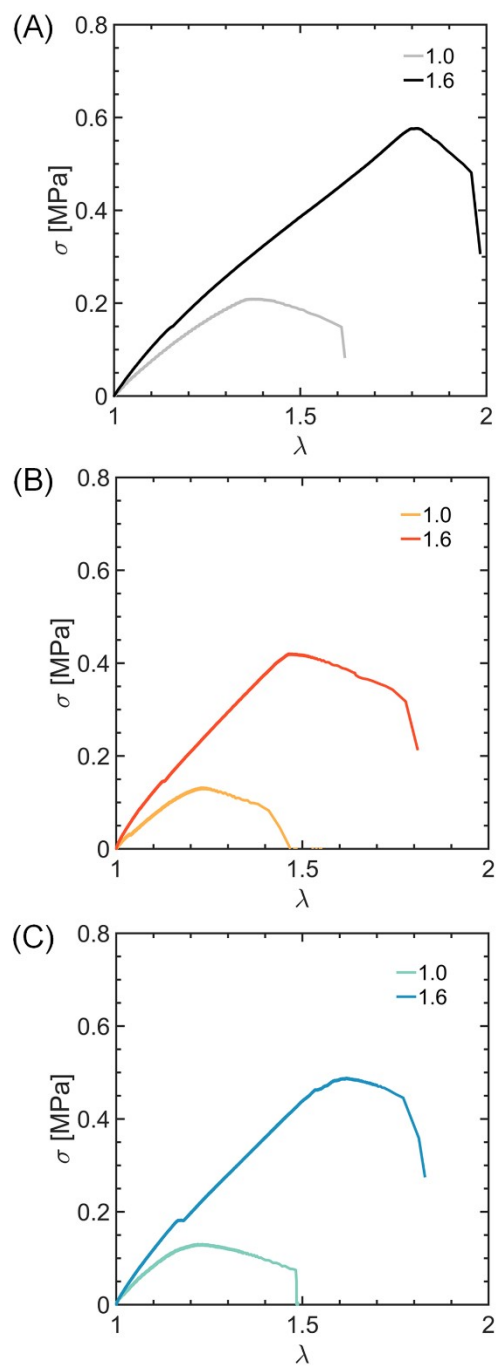


Figure S4. Stress-stretch curves of filler ($\lambda_0 = 1.0$) and multiple-networks ($\lambda_0 = 1.6$) in single-edge notch fracture tests ($T = 23^\circ\text{C}$ and $\dot{\lambda} = 0.003\text{s}^{-1}$), for filler networks synthesized by (A) free radical (B) RAFT and (C) ATRP copolymerizations. Embedding pre-stretched filler network chains within a multiple-network architecture leads to toughening.

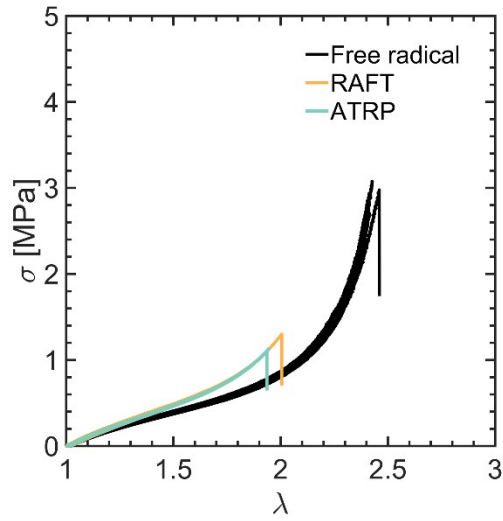


Figure S5. Stress-stretch curves of multiple-networks under step-cyclic loads. Irrespective of filler network architecture, all three multiple-networks are nearly perfectly elastic, showing no hysteresis under the loading-unloading curves.

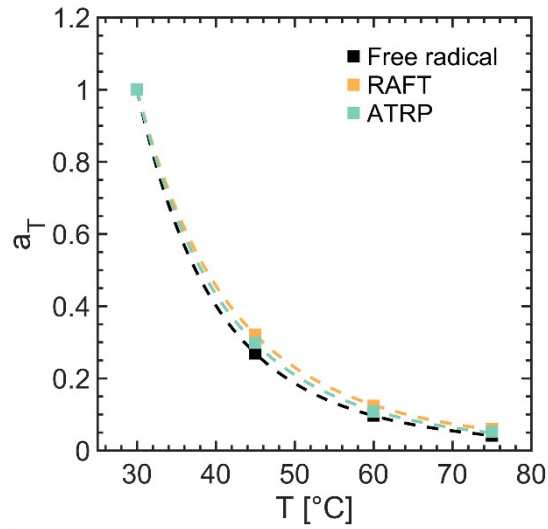


Figure S6. Viscoelastic shift factors of multiple-networks. Irrespective of the filler network architecture, all three multiple-networks show similar time- and temperature-dependence in rheology.

Rate- and temperature-dependent fracture of multiple-networks

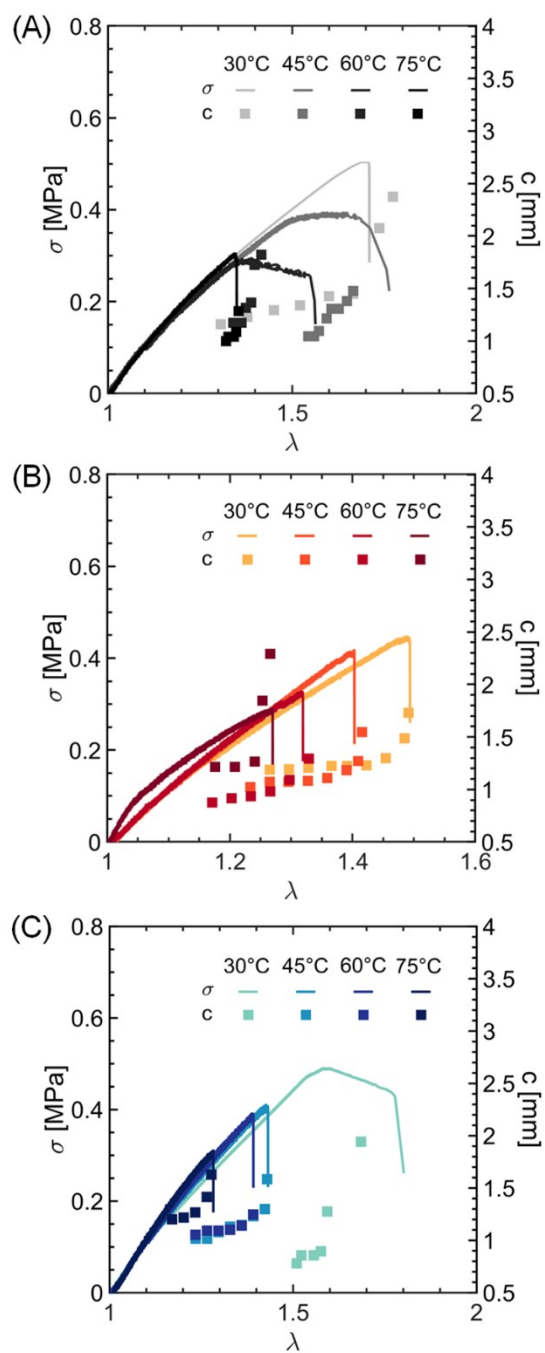


Figure S7. Stress-stretch curves and crack length from single-edge notch fracture tests conducted in multiple-networks at various temperatures. The filler networks in these multiple-networks were synthesized by (A) free radical, (B) RAFT and (C) ATRP. Higher temperatures promoted fracture.

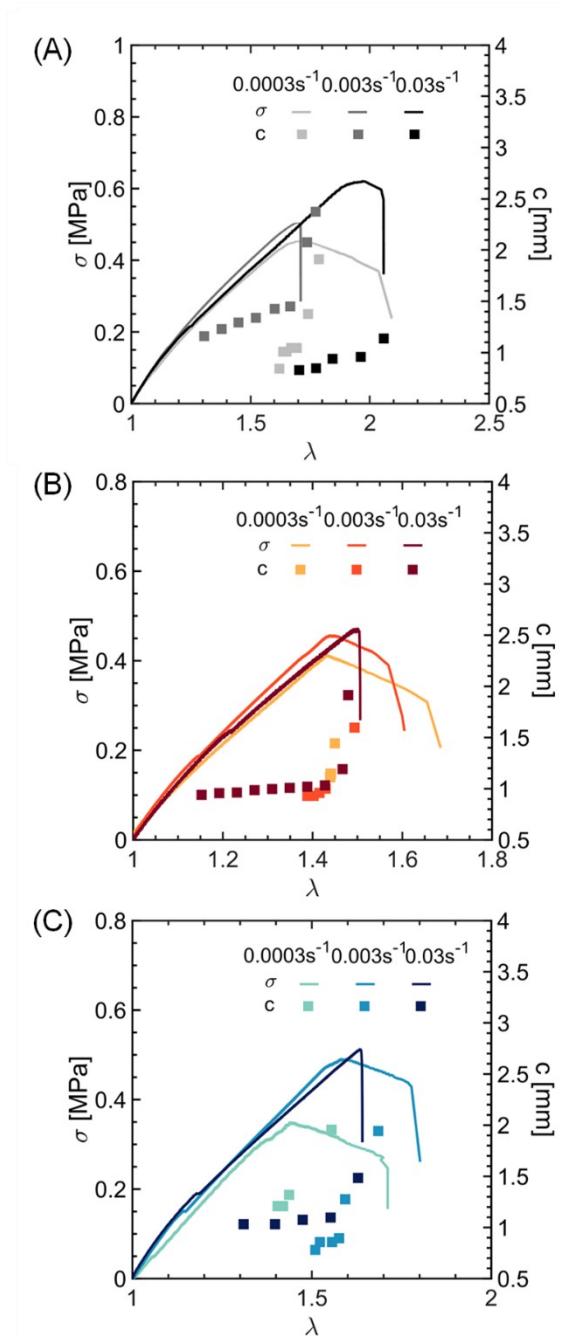


Figure S8. Stress-stretch curves and crack length from single-edge notch fracture tests conducted in multiple-networks at various loading rates. The filler networks in these multiple-networks were synthesized by (A) free radical, (B) RAFT and (C) ATRP. Higher rates delayed fracture.

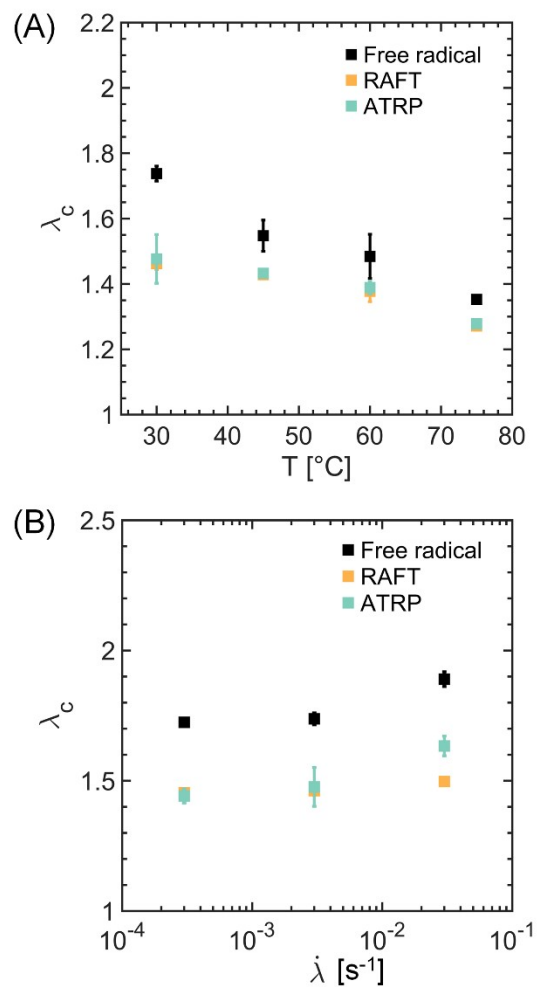


Figure S9. Critical stretch for crack propagation in single-edge notch fracture tests of multiple-networks under varying (A) temperatures and (B) stretch rates. The critical stretch increases in conditions of favorable viscoelastic dissipation, such as high rates and low temperatures. Under most conditions, multiple-networks with filler networks synthesized by RAFT and ATRP exhibit a lower critical stretch than those composed of filler networks synthesized by free radical polymerization.

Table S2. Single-edge notch fracture tests in multiple-networks: crack length, c , critical stretch, λ_c , strain energy density, $W(\lambda_c)$, and fracture toughness, G_c .

Mechanism	T [°C]	λ [s^{-1}]	c [mm]	λ_c	$W(\lambda_c)$ [10^5 Jm^{-3}]	G_c [Jm^{-2}]
FRP	30	0.0003	0.96 ± 0.10	1.72 ± 0.06	1.94 ± 0.03	850 ± 49
	30	0.003	1.31 ± 0.08	1.74 ± 0.05	2.02 ± 0.26	1200 ± 37
	30	0.03	1.04 ± 0.04	1.89 ± 0.06	3.45 ± 0.22	1500 ± 48
	45	0.003	1.09 ± 0.09	1.55 ± 0.10	1.54 ± 0.11	870 ± 36
	60	0.003	1.19 ± 0.20	1.48 ± 0.14	0.80 ± 0.14	460 ± 6
	75	0.003	1.13 ± 0.13	1.35 ± 0.05	0.63 ± 0.07	360 ± 50
RAFT	30	0.0003	0.85 ± 0.05	1.45 ± 0.02	0.99 ± 0.03	420 ± 17
	30	0.003	1.29 ± 0.04	1.46 ± 0.04	1.15 ± 0.03	740 ± 38
	30	0.03	1.50 ± 0.05	1.50 ± 0.01	1.30 ± 0.05	950 ± 21
	45	0.003	1.14 ± 0.11	1.42 ± 0.01	0.96 ± 0.15	540 ± 40
	60	0.003	1.02 ± 0.18	1.38 ± 0.06	0.82 ± 0.21	410 ± 38
	75	0.003	1.28 ± 0.07	1.27 ± 0.01	0.44 ± 0.02	300 ± 1
ATRP	30	0.0003	1.09 ± 0.28	1.44 ± 0.05	1.03 ± 0.20	530 ± 110
	30	0.003	1.50 ± 0.50	1.48 ± 0.15	1.19 ± 0.51	760 ± 52
	30	0.03	1.14 ± 0.12	1.63 ± 0.08	1.57 ± 0.22	840 ± 12
	45	0.003	1.34 ± 0.02	1.43 ± 0.01	0.99 ± 0.03	660 ± 31
	60	0.003	1.37 ± 0.01	1.42 ± 0.04	0.81 ± 0.04	560 ± 40
	75	0.003	1.24 ± 0.12	1.28 ± 0.01	0.50 ± 0.08	380 ± 77

Table S3. Crack propagation velocities, v , in multiple networks with different filler networks, measured under varying rates and temperatures.

T [°C]	λ [s^{-1}]	v_{FRP} [mm.s^{-1}]	v_{RAFT} [mm.s^{-1}]	v_{ATRP} [mm.s^{-1}]
30	0.003	0.15	0.11	0.16
45	0.003	0.22	0.14	0.19
60	0.003	0.076	0.13	0.22
75	0.003	0.085	0.13	0.16
30	0.0003	0.017	0.017	0.016
30	0.03	1.3	0.47	0.44

Polymer mechanochemistry

Table S4. Synthesis of mechanophore-labeled polymer networks by free radical, RAFT and ATRP copolymerization.

Mechanism	EA			BDA			DACL		Initiator (HMP or EBiB)			CTA or Copper	
	x [mol%]	V [mL]	m [g]	x [mol%]	V [mL]	m [g]	x [mol%]	m [mg]	x [mol%]	V [mL]	m [g]	x [mol%]	m [g]
FRP	99.4	3	2.8	0.48	0.02 6	0.0 3	0.02	3.1	0.1	0.00 4	0.00 5	-	-
RAFT	98.9	3	2.8	0.98	0.05 3	0.0 6	0.02	3.1	0.02	0.00 1	0.00 1	0.1	0.009
ATRP	98.9	3	2.8	0.98	0.05 3	0.0 6	0.02	3.1	0.07	0.00 3	0.00 4	0.007	0.000 3

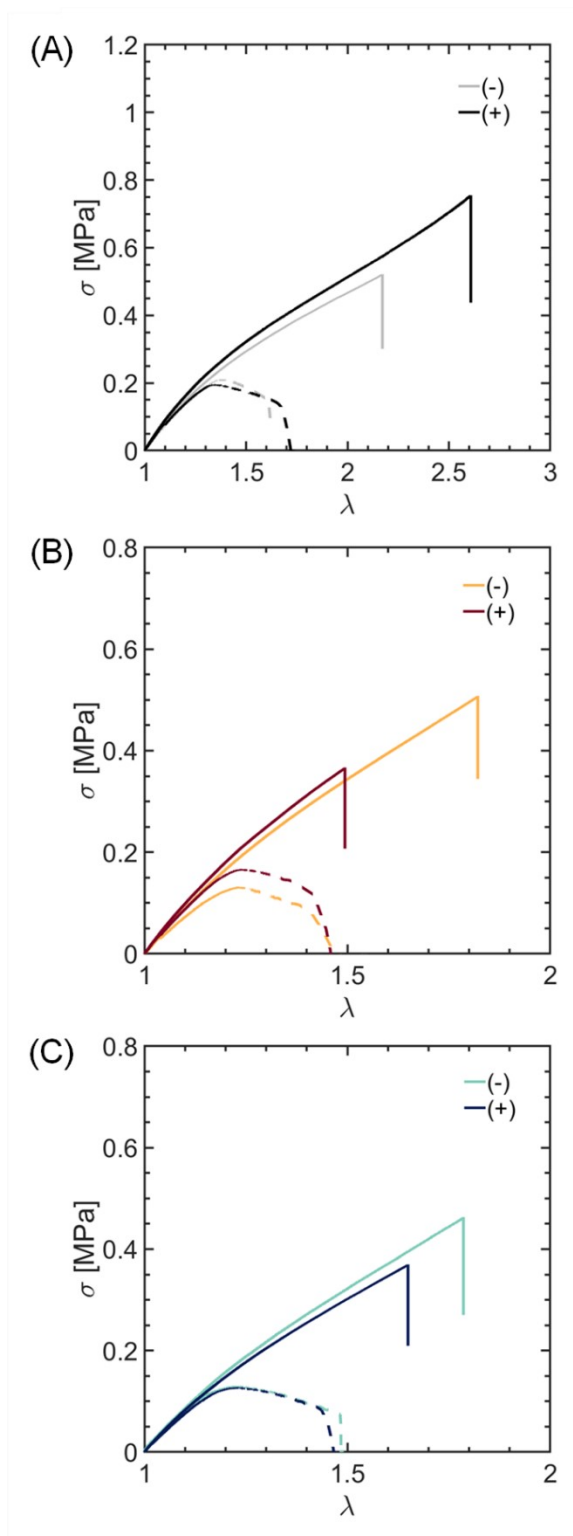


Figure S10. Mechanical properties of filler networks without (-) and with (+) mechanophore, synthesized by (A) free radical, (B) RAFT and (C) ATRP polymerizations. The presence of mechanophores does not significantly affect the elastic modulus and fracture toughness. Solid and dashed lines correspond to un-notched and notched specimens, respectively.

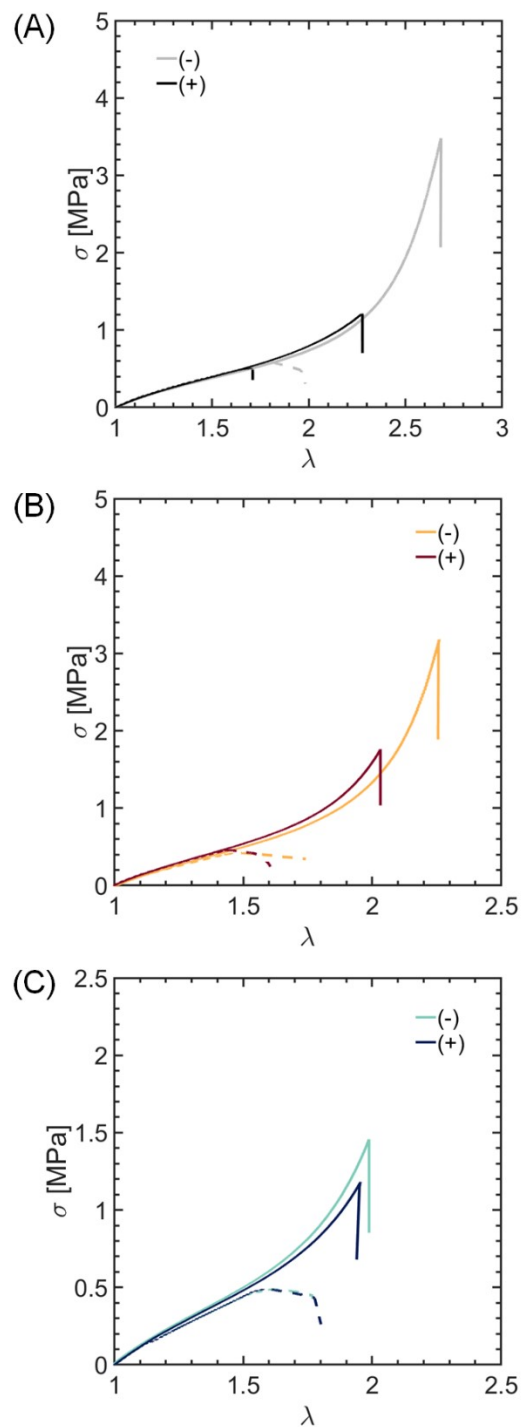


Figure S11. Mechanical properties of multiple networks made from filler networks without (-) and with (+) mechanophore. These filler networks were synthesized by (A) free radical, (B) RAFT and (C) ATRP copolymerizations. The presence of mechanophores in the filler networks does not significantly affect the elastic modulus or the fracture toughness of the multiple-networks. Solid and dashed lines correspond to un-notched and notched specimens, respectively.

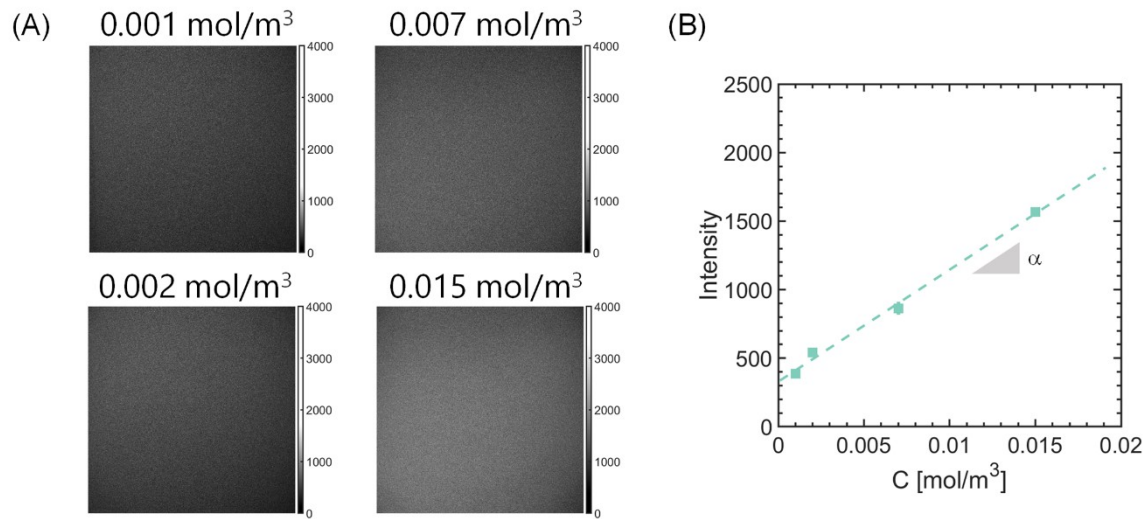


Figure S12. Calibration of fluorescence intensity. (A) Fluorescence intensity increases with the fluorophore concentration. (B) Representative calibration curve illustrates a linear relationship between fluorescence intensity and fluorophore concentration, with the slope of the line denoted as α .

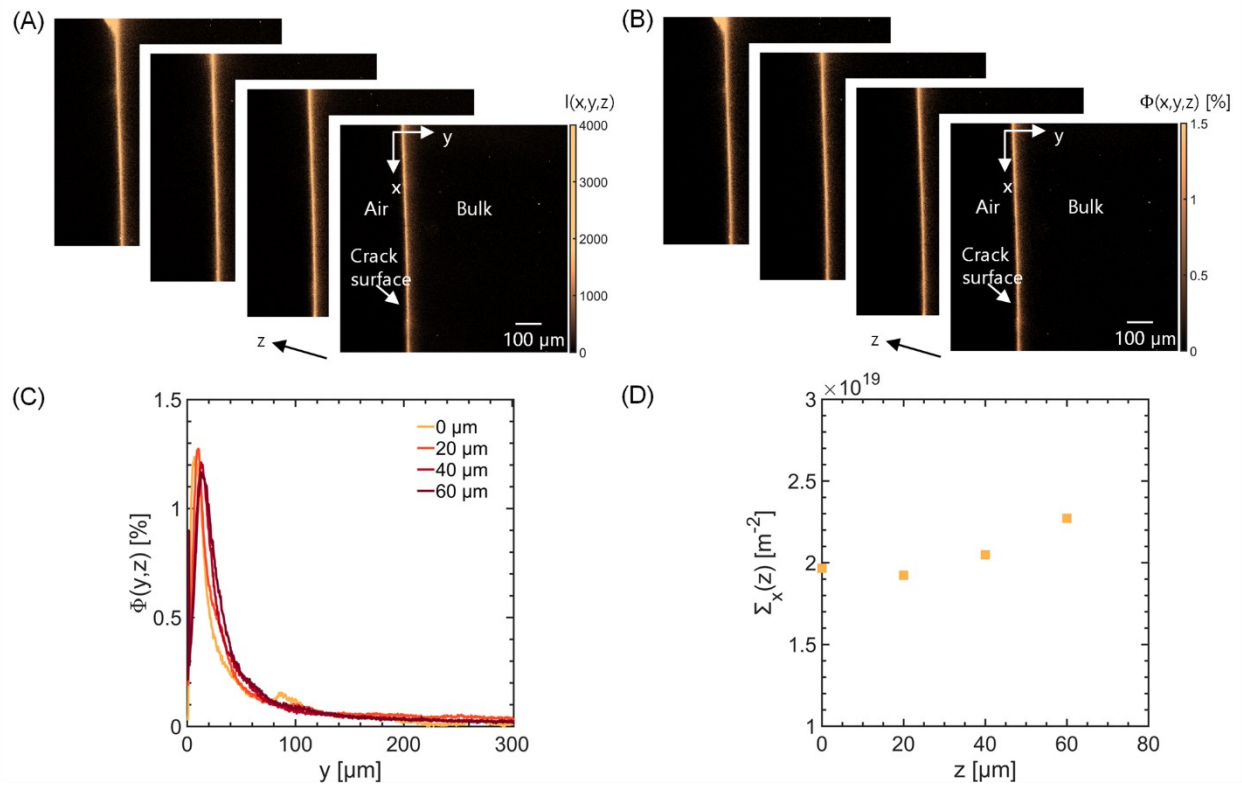


Figure S13. Image processing and confocal imaging of fractured specimens. (A) Confocal images revealing fluorescence, $I(x,y,z)$, captured at various imaging planes, indicating mechanophore activation and chain breakage along the crack surface. (B) Corresponding maps of the fraction of activated mechanophores, $\Phi(x,y,z)$, estimated from Eq. 6 and the calibration curve in Fig. S12. (C) Damage profiles obtained by averaging the fraction of activated mechanophores, $\Phi(x,y,z)$, along the crack propagation direction, x , at different imaging planes, z . (D) Areal density of activated mechanophores, Σ_x , estimated by integrating the damage profiles, $\Phi(y,z)$, along the penetration direction, y , for each z -plane.

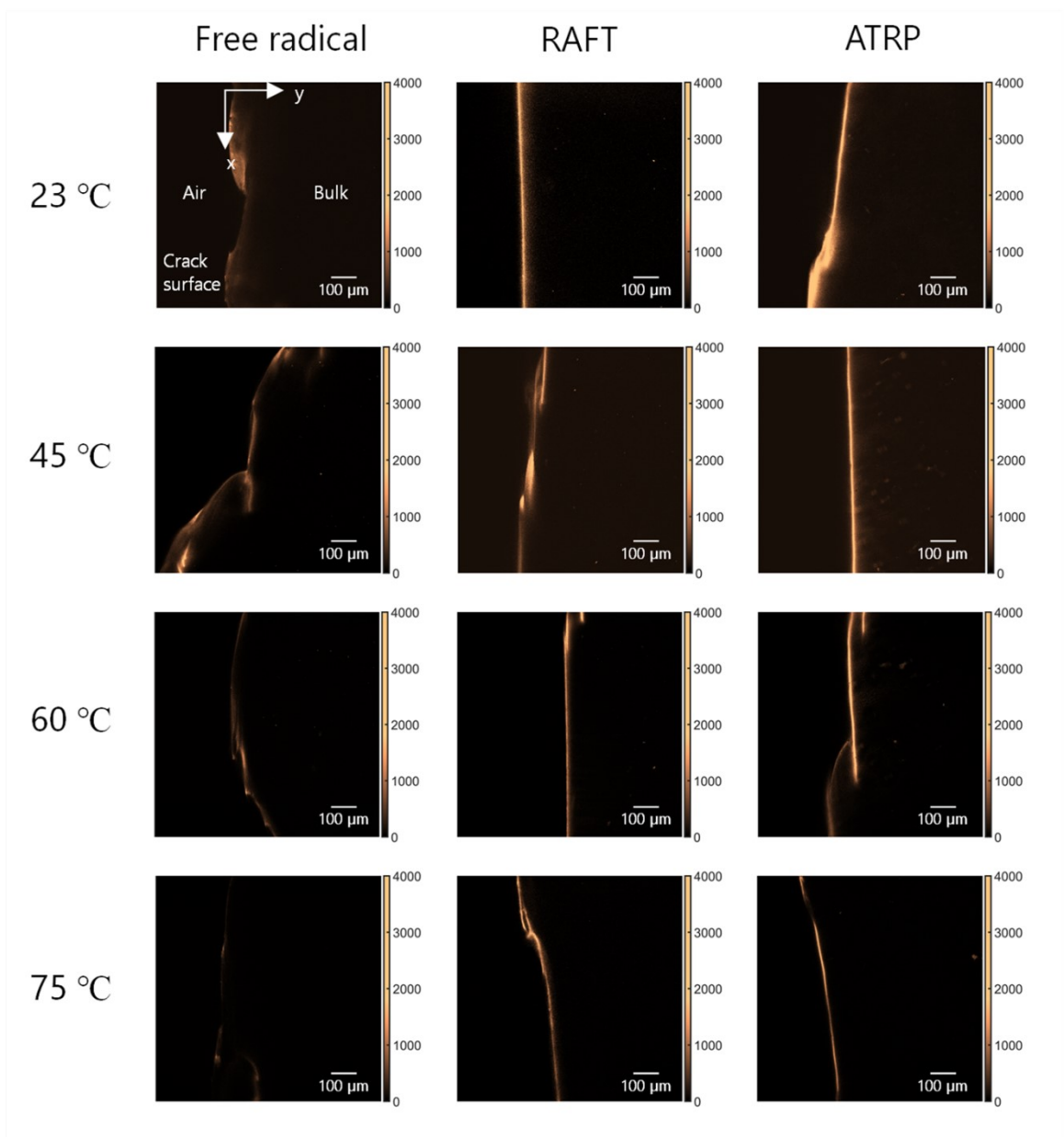


Figure S14. Representative crack surfaces of multiple networks (i) containing filler networks synthesized by free radical, RAFT and ATRP polymerizations and (ii) fractured at different temperatures. Regardless of the gelation method used to synthesize the filler network, the fluorescence intensity decreases with increasing temperature.

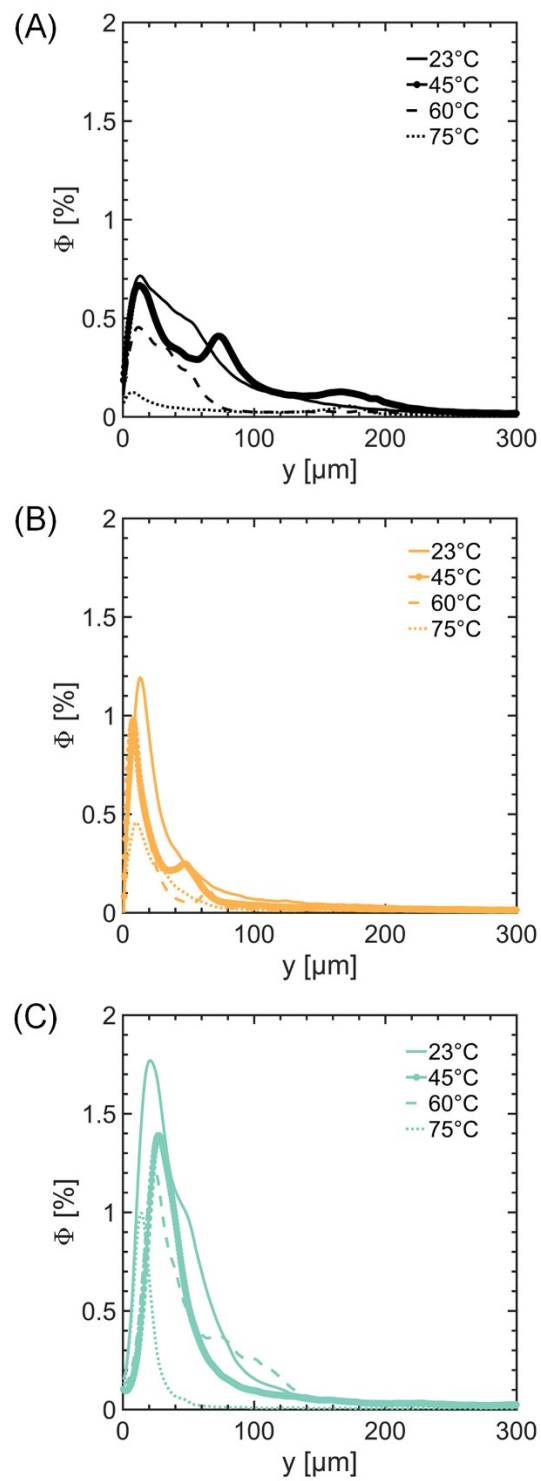


Figure S15. Fraction of activated mechanophores in multiple networks (i) containing filler networks synthesized by free radical, RAFT, and ATRP polymerizations and (ii) fractured at different temperatures. The extent of damage decreases with increasing temperature, regardless of the gelation method used to synthesize the filler network.

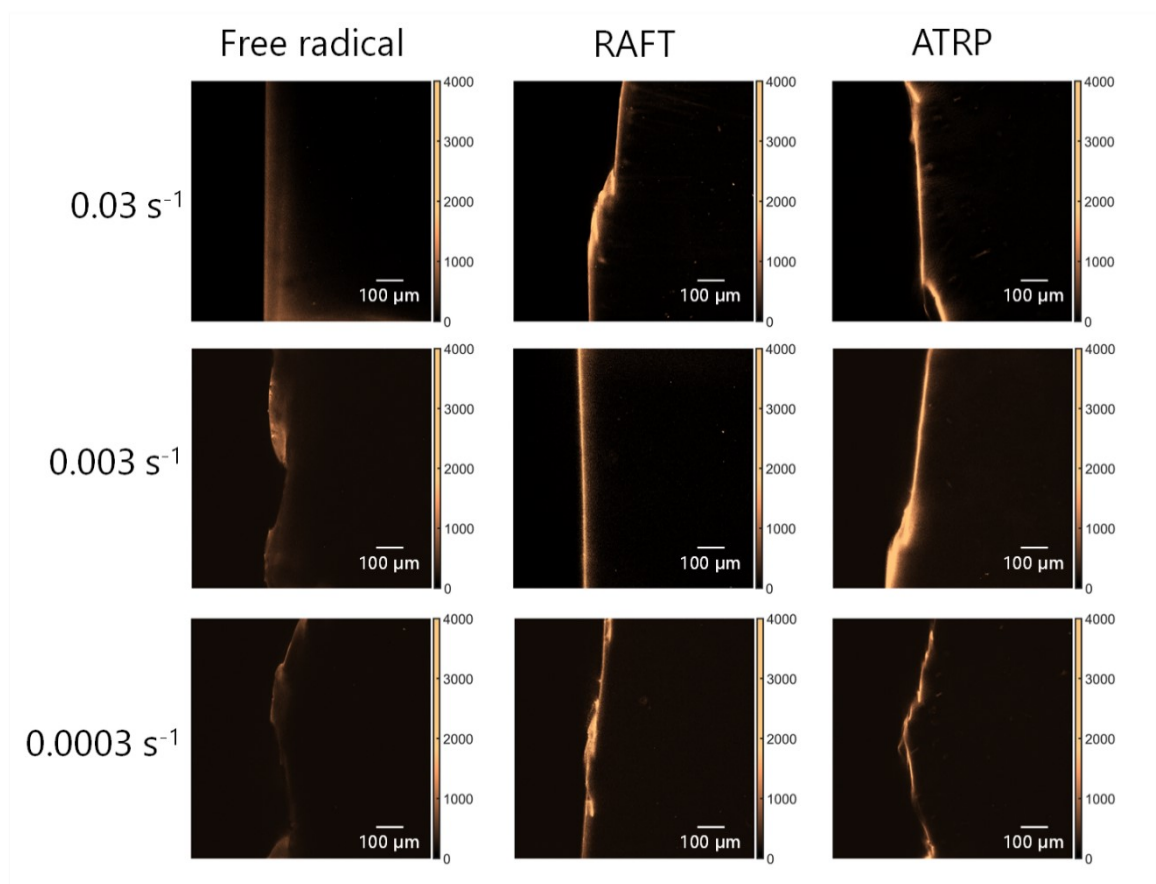


Figure S16. Representative crack surfaces of multiple networks (i) containing filler networks synthesized by free radical, RAFT and ATRP polymerizations and (ii) fractured at different rates. Regardless of the gelation method used to synthesize the filler network, the fluorescence intensity decreases with reduced rate.

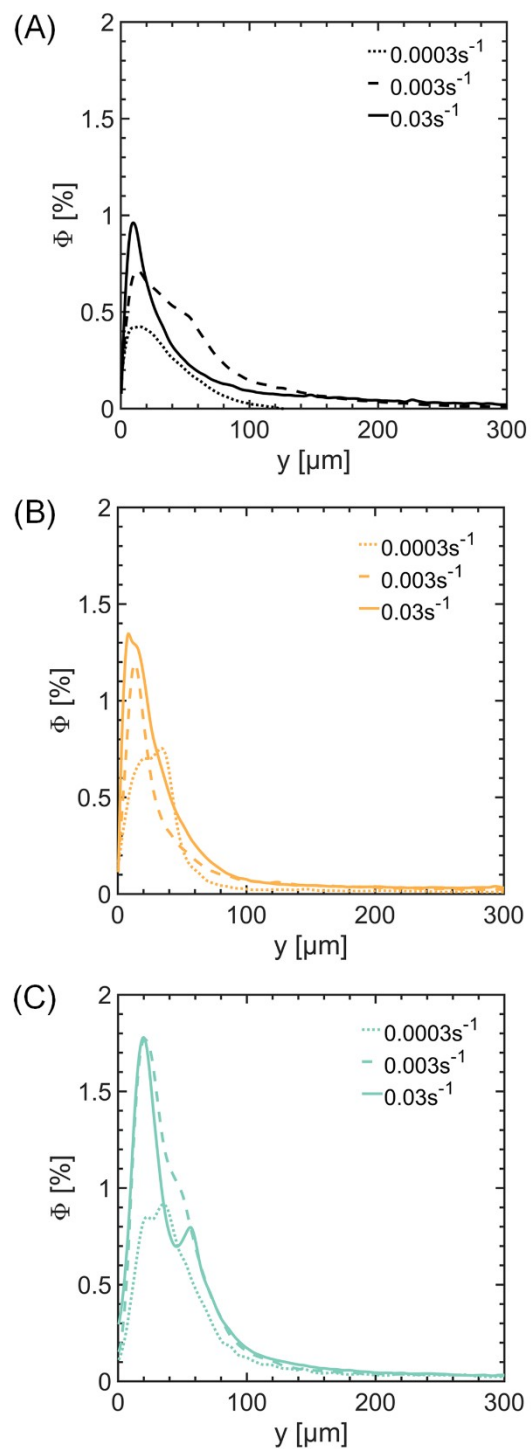


Figure S17. Fraction of activated mechanophores in multiple networks (i) containing filler networks synthesized by free radical, RAFT and ATRP polymerizations and (ii) fractured at different rates. Regardless of the gelation method used to synthesize the filler network, the extent of damage decreases with reduced rate.

Bifurcations along the crack surfaces of all multiple-networks led to multiple peaks in the damage profiles, complicating the estimation of a characteristic length scale for damage delocalization. For simplicity, the damage delocalization length scale was determined by analyzing regions of the crack surface where the crack grew without bifurcating (see example in **Fig. S18A**). These regions offered the damage delocalization length scale, $L_{0.9}$ (see dashed line in **Fig. S18B**).

Consistent with measurements of the damage extent, Σ , “filler” networks synthesized by RAFT and ATRP exhibited more localized damage than that synthesized by FRP across the entire range of rates and temperatures (see **Fig. S19**).

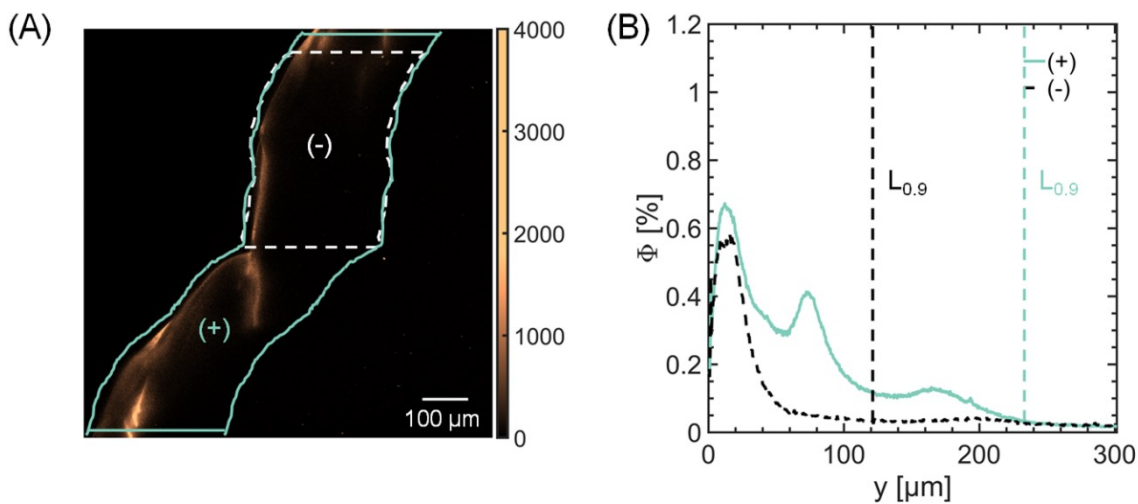


Figure S18. Estimates of damage localization. (A) Representative confocal image of a multiple-network, based on a filler network synthesized by FRP, fractured at 45 °C and 0.03 s⁻¹. The image reveals bifurcations near the fracture surface, resulting from crack nucleation events occurring prior to crack growth (B) Damage profile in the region-of-interest (ROI) with (+) and without (-) bifurcations. Accounting for bifurcations clearly introduces secondary and tertiary peaks, which significantly influence the estimation of the damage delocalization length scale, $L_{0.9}$.

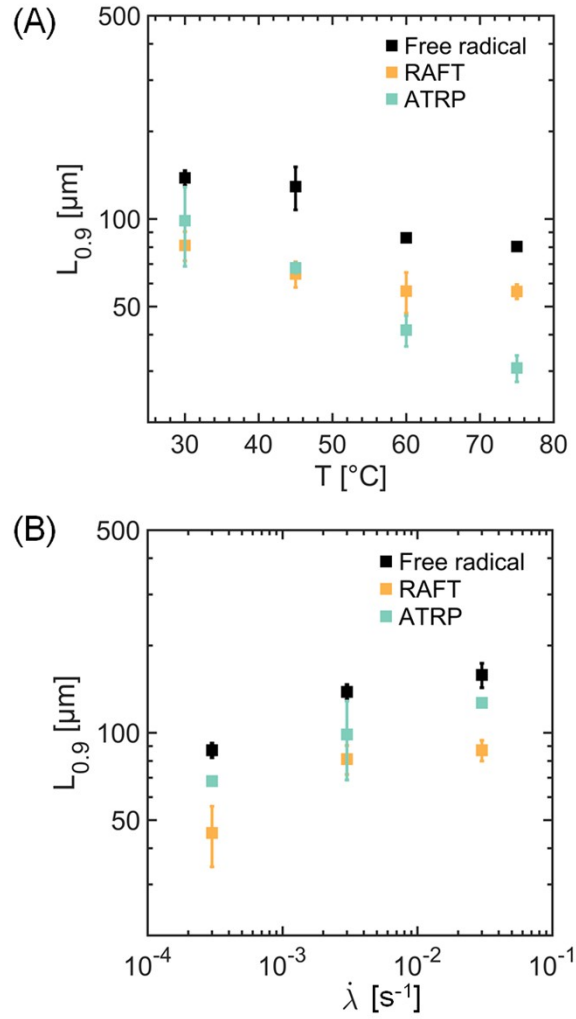


Figure S19. Damage localization in multiple-networks fractured at varying (A) temperatures and (B) rates. Clearly, filler-networks synthesized by FRP are more effective at delocalizing damage than those synthesized by RAFT and ATRP, exhibiting a larger delocalization length scale, $L_{0.9}$ across a range of rates and temperatures.

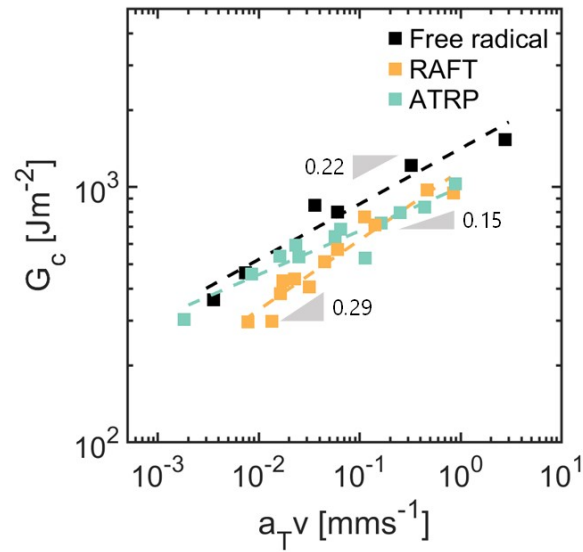


Figure S20. Fracture toughness as function of the reduced crack propagation velocity. Under similar viscoelastic conditions, filler networks synthesized by free radical polymerization result in somewhat tougher networks than those synthesized by RAFT and ATRPs.

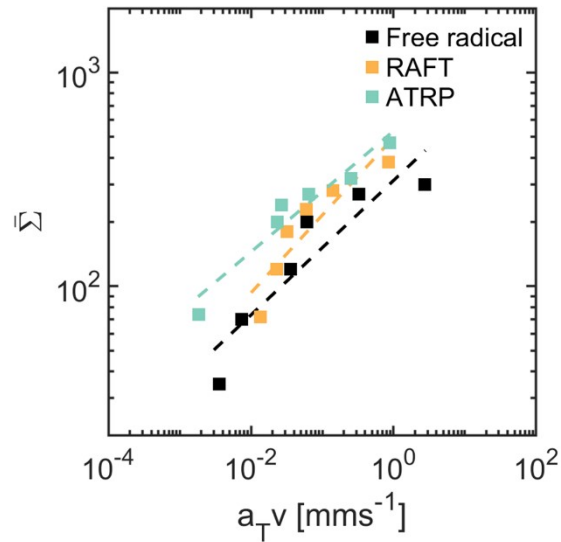


Figure S21. Damage as a function of the reduced crack propagation velocity. Under similar viscoelastic conditions, filler networks synthesized by RAFT and ATRP result in larger damage zones than those synthesized by free radical polymerization.

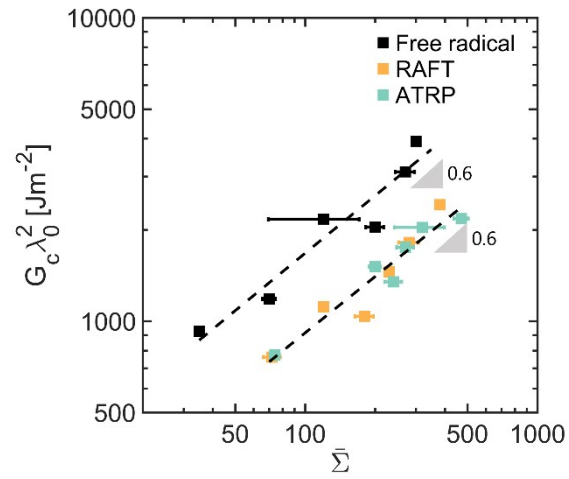


Figure S22. Scaling behavior of the fracture toughness with respect to the damage zone size. Irrespective of the gelation method used to synthesize the filler network, the multiple networks show similar scaling exponent of 0.6 indicative of a coupling between viscoelasticity and damage ahead of the crack.

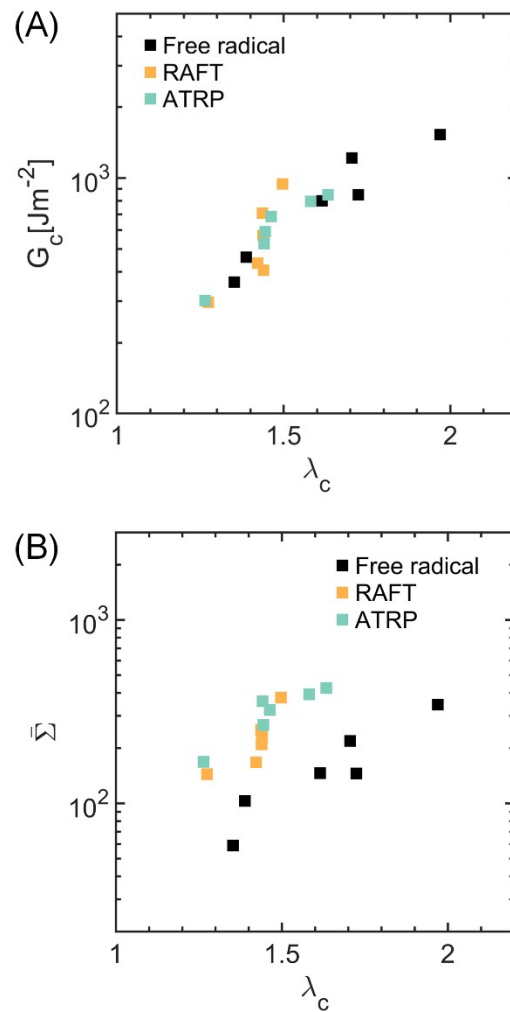


Figure S23. Molecular picture of fracture in multiple-networks containing filler networks synthesized by free radical, RAFT and ATRP. **(A)** Fracture toughness increases with critical stretch as a result of viscoelastic dissipation ahead of the crack. **(B)** Higher strains, both in the bulk and at the crack front, results in more extended filler network chains and higher probabilities of filler network breakage. Filler networks obtained from RAFT and ATRPs experience more damage due to their narrowly dispersed elastic chains, which readily concentrate stress and break. However, they dissipate less energy as the broken filler network chains are, on average, shorter.

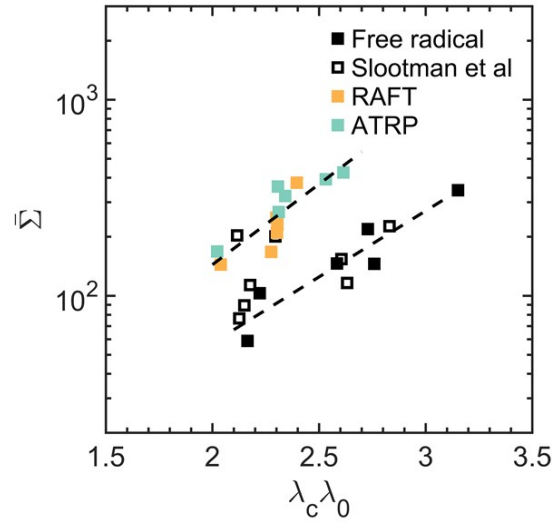


Figure S24. Damage increases with the critical stretch within the filler network but depends on the synthesis method. Networks synthesized by RAFT and ATRP, which have narrower distributions of chain lengths and are on average less extensible, experience more damage than those synthesized by free radical polymerization. Empty squares reproduced from Sootman *et al.*¹ Two master curves with similar slopes result, with FRP $\approx 1.6 \pm 0.8$, and RAFT and ATRP $\approx 1.9 \pm 0.8$.

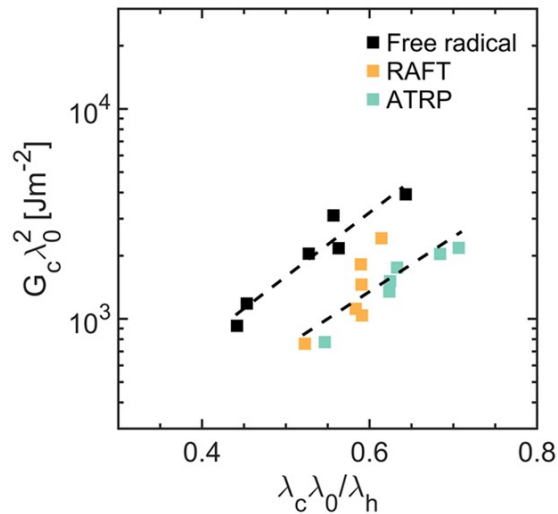


Figure S25. Toughness increases with the critical stretch within the filler network. However, the synthesis method – FRP, RAFT, and ATRP - plays an important role in energy dissipation. Filler networks synthesized by RAFT and ATRP offer less dissipative multiple-networks than those synthesized by free radical polymerization due to their narrower chain length distributions in the load-bearing phase. Two master curves with similar slopes result, with FRP $\approx 7.0 \pm 2.8$, and RAFT and ATRP $\approx 6.0 \pm 3.1$.

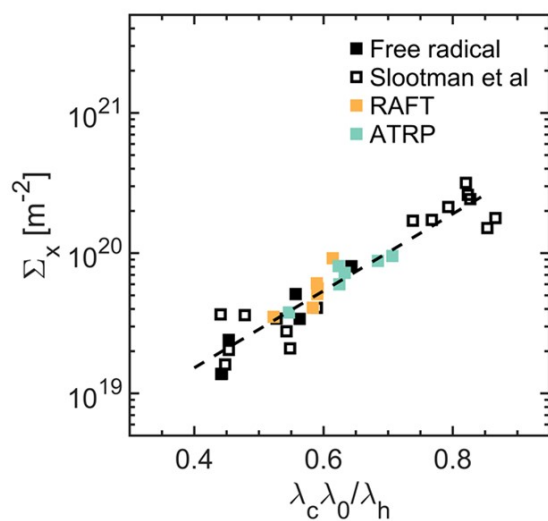


Figure S26. Damage increases with the critical stretch within the filler network, collapsing onto a master curve when renormalized by the average extensibility of the filler network chains. Highly pre-stretched chains result in more damage, consistent with the picture postulated by Sootman *et al.*¹ Slope of the line $\approx 6.3 \pm 1.2$.

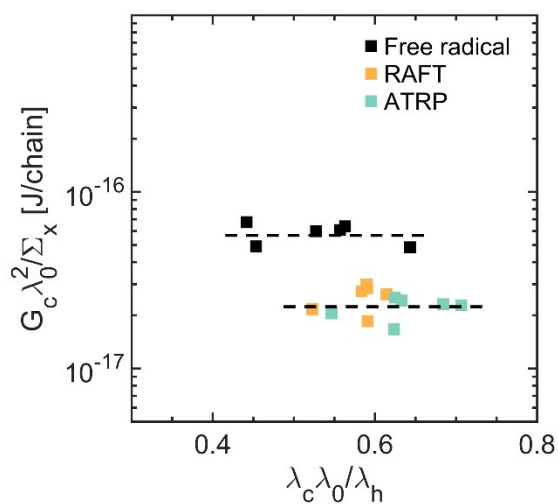


Figure S27. Energy dissipated per broken filler network chain depends on the polymerization method used to synthesize the filler network. RAFT and ATRP lead to filler networks with a higher fraction of short chains, which dissipate less energy when they elongate to their contour length and break.

Optical properties of multiple networks

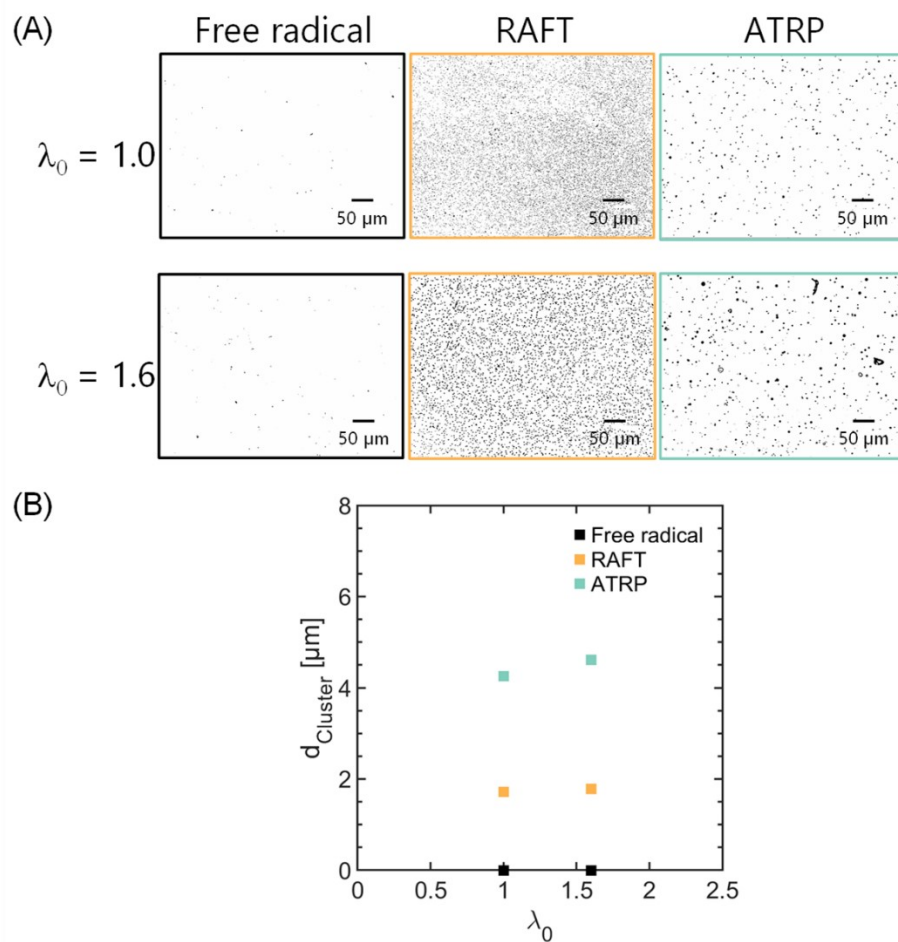


Figure S28. Phase separation in filler networks synthesized by free radical, RAFT and ATRP. (A) Filler networks synthesized by RAFT and ATRP, along with their corresponding multiple-networks, exhibit phase separation and appear opaque. (B) Based on optical microscope, these networks feature clusters that locally pre-stretch to $\lambda_0 \sim 1.1$, even though the bulk pre-stretched to $\lambda_0 \sim 1.6$.

MODELS AND CALCULATIONS

Volume fraction and pre-stretch of the filler networks

The properties of multiple-network elastomers notably depend on the volume fraction, ϕ_0 , or isotropic pre-stretch, λ_0 , of the filler network. This pre-stretch was estimated from the mass of the single- (*i.e.*, filler) and the multiple-networks using the following relation:

$$\phi_0 = \left(\frac{m_{FN}}{m_{MN}} \right) = \lambda_0^{-1/3} \quad (\text{Eq. S1})$$

Where m_{FN} and m_{MN} are the mass of the filler- and multiple-networks, respectively.

SIMULATION DETAILS

Reactive Monte-Carlo Simulations

The 3-dimensional bond fluctuation model (3DBFM) was used to perform the copolymerization reactions². The free radical copolymerization (FRP) consisted of three modules: initiation, propagation, and termination. The reaction probabilities for the three modules are listed in Table S5, where k_i is the reaction probability for initiation, k_{p1} for a propagating radical to react with mono- or unreacted di-vinyl monomers, k_{p2} for a propagating radical to react with partially reacted di-vinyl monomer (pendant group), and k_t is for termination by recombination (disproportionation is not considered).

Based on Furuya and Koga's work, we set $k_{p2}=0.5 k_{p1}$ ³. This choice ensured that initiation was sufficiently slow compared to propagation, in line with the kinetics of FRP, and did not influence the topological differences among the networks. In addition, we adopted $k_t \geq k_p$, which is different from the expected $k_t \gg k_p$ but ensures computational tractability^{3,4}.

For the RAFT copolymerization, no initiation reaction occurred due to the fast initiation rate of the polymerization. Instead, the maximum allowed number of propagating chains R^* was available for propagation (with reaction probabilities k_{p1}/ k_{p2}) or termination at the start of the polymerization. The deactivation/activation reactions were considered implicitly; an approach successfully used in several reports^{2,5,6}.

Similar to the RAFT copolymerization, the ATRP did not feature an initiation reaction, and all potential propagating chains R^* were available for propagation at the beginning of the simulation. Moreover, due to the extremely low concentration of living radicals, no termination reaction occurred.

Table S5. Parameters used to simulate free radical, RAFT and ATRP copolymerizations: R^* is the concentration of propagating chains in the system, k_i is the probability of initiation, k_{p1} is the probability of forming a first bond, k_{p2} is the probability of forming a second bond, and k_t is the probability of termination².

Mechanism	R^* [mol%]	k_i	k_{p1}	k_{p2}	k_t
FRP	0.2	10^{-6}	0.5	0.25	0.9
RAFT	0.2	-	0.05	0.025	0.005
ATRP	0.2	-	0.05	0.025	-

The lattice box dimension was $100 \times 100 \times 100$ for all three copolymerizations. The total number of monomers and radicals was set to 106,250, which corresponded to a polymer melt number density of 0.85. All initiators/radicals and monomers were initially randomly distributed within the lattice.

Each Monte-Carlo Step (MCS), representing the timescale of our simulation, involved 106,250 random monomer selections for position updates. Following each update, if the selected monomer encountered a suitable reactant within its 54 nearest neighbors, a random number was generated and compared to the corresponding reaction probability. If the random number was smaller, the reaction (*e.g.*, initiation, propagation, or termination) occurred.

The copolymerizations were performed until the vinyl group conversion reached 98%. Subsequently, unreacted radicals and monomers were removed, and the resulting polymer network was mapped onto a coarse-grained representation. Importantly, the number density was maintained at $0.85 \sigma^{-3}$, where σ is the diameter of a coarse-grained bead.

Graph theory was used for topology analysis, specifically to determine the number density of elastically active chains within the networks. In this approach, monomers in the network were treated as nodes (or vertices), and the bonds between them as edges. An elastically active chain was defined as the unique path between two effective crosslinkers, where the monomers along this path have a functionality of 2. Effective crosslinkers were identified based on the Scanlan-Case criterion; that is, considering a monomer as an effective crosslinker if it connected more than two elastically active strands^{7,8}. This analysis was performed using an in-house code that utilizes the NetworkX library⁸.

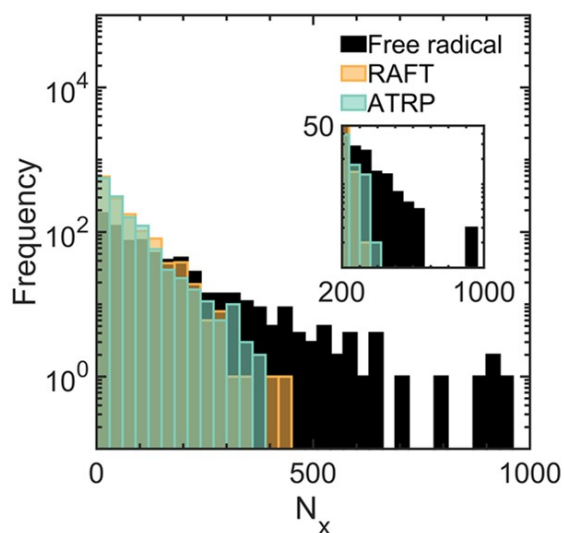


Figure S29. Chain length distributions in the load-bearing phase of the filler networks synthesized by FRP, RAFT, and ATRP. These distributions were estimated from reactive Monte-Carlo simulations using the procedure outlined in Dookhith et al. and Zhang et al.^{2,9}

Coarse-Grained Molecular Dynamics Simulations

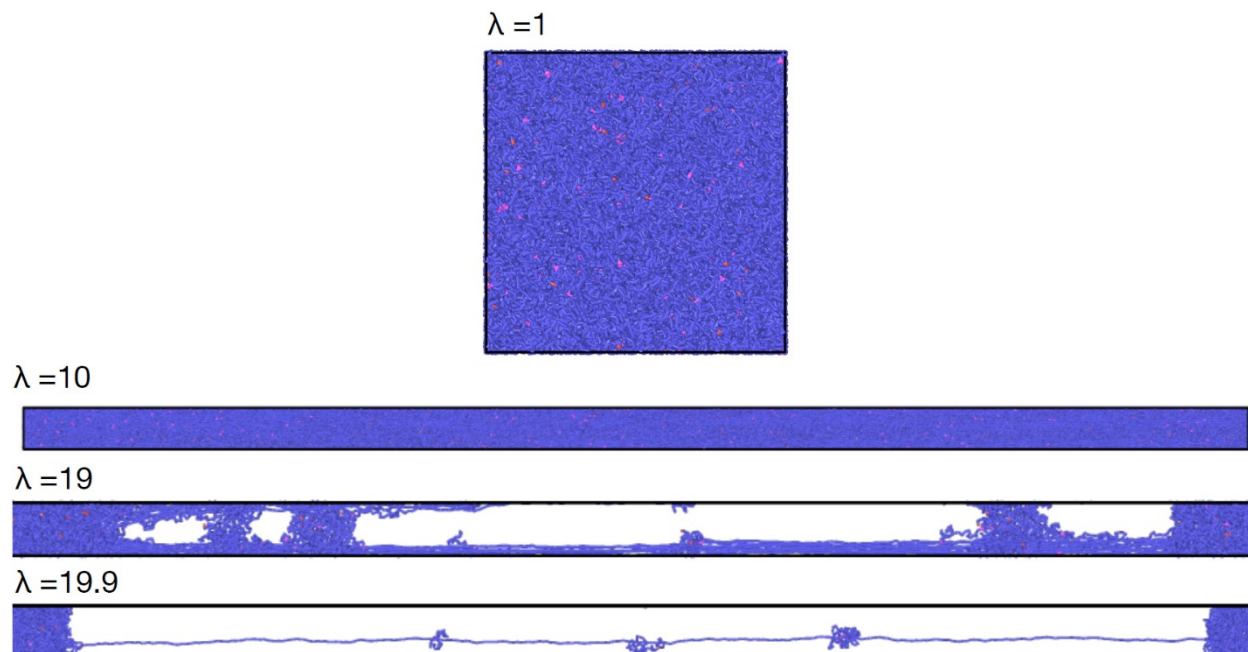


Figure S30. Snapshots for the polymer network prepared through ATRP during uniaxial deformation at $\lambda = 1, 10, 19$ and 19.9 . The last two snapshots only zoom in on the ruptured area. The network fully breaks past $\lambda = 19.9$.

During the equilibration period, prior to deformation and under an NPT ensemble, the temperature and pressure were set to $T = 1.5$ and $P = 1.0$, respectively. This state ensured that the number density of all three systems was maintained around $0.85 \sigma^{-3}$, as illustrated in **Fig. S31**.

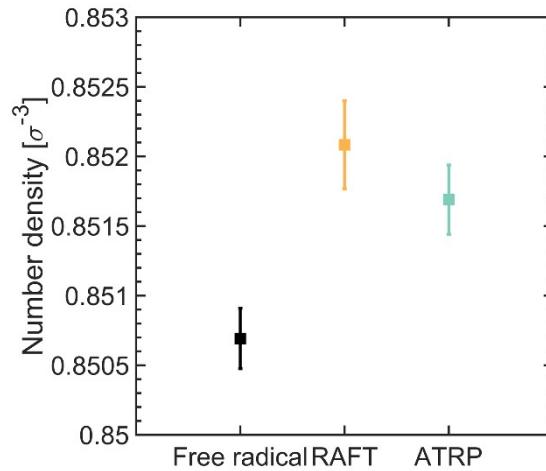


Figure S31. The number density of equilibrated polymer network before deformation, during the equilibration, the breakable quartic bond potential is applied.

For the uniaxial deformation, an elongation rate of $5 \times 10^{-5} \tau^{-1}$ was used. The stretch ratio, λ , was defined as L/L_0 , where L and L_0 were the box lengths in the deformed and undeformed configurations, respectively. The engineering stress, σ , was defined as:

$$\sigma = \frac{-P_{xx}}{\lambda} \quad (\text{Eq. S2})$$

where P_{xx} is the pressure tensor in the loading direction, x .

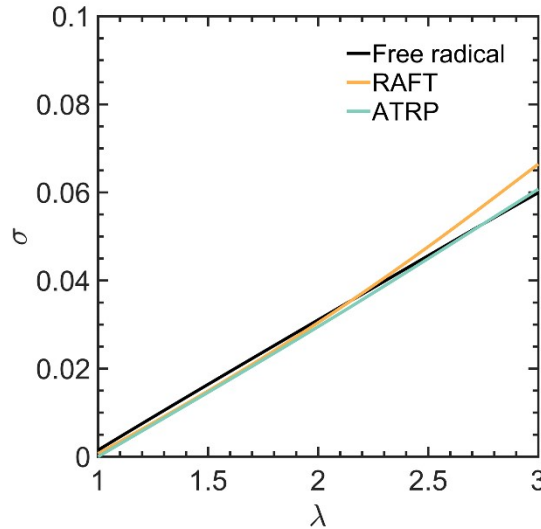


Figure S32. The linear regression of the initial part of stress-strain curve for Young's modulus, the solid lines represent the fits. The slopes for FRP, RAFT and ATRP systems are 0.0314, 0.0361 and 0.0317, respectively.

Consistent with experimental observations, the three simulated networks had the same elastic modulus in the simulations, as shown in **Fig. S32**.

The coarse-grained molecular dynamics simulations enabled the study of the failure process at a molecular scale, with a focus on chain scission events. These chain scission events were characterized as either random or correlated based on the distance between them as a function of the stretch ratio, λ . In monitoring these events, the stretch ratio was divided into 8 bins, each with a size of 1.5. Within each bin, the shortest distance of a scission event to all other events was calculated based on the spatial coordinates.

Given a coarse-grained simulation box length of about 49σ , we created four distance intervals ranging from 0 to 20σ (less than half the box length), with an increment of 5σ . The calculated shortest distances between chain scission events were then categorized into these four intervals, as shown in **Fig. S33**.

We observed that the network obtained via FRP exhibited a delayed failure process compared to analogous networks synthesized via RAFT and ATRP. The sharp increase in chain scission events occurred around $\lambda = 9$ for FRP, whereas it occurred around $\lambda = 7.5$ for RAFT and ATRP.

Moreover, at the onset of deformation, chain scission events occurred throughout the network, as the fraction of closest distances was similar across all distance intervals. However, as the deformation increased, the count and fraction of closest distances in the higher intervals ($[10, 15] \sigma$ and $[15, 20] \sigma$) decreased, while they increased in the shorter intervals ($[0, 5] \sigma$ and $[5, 10] \sigma$). This observation suggests a transition from randomly distributed chain scission events to spatially correlated ones.

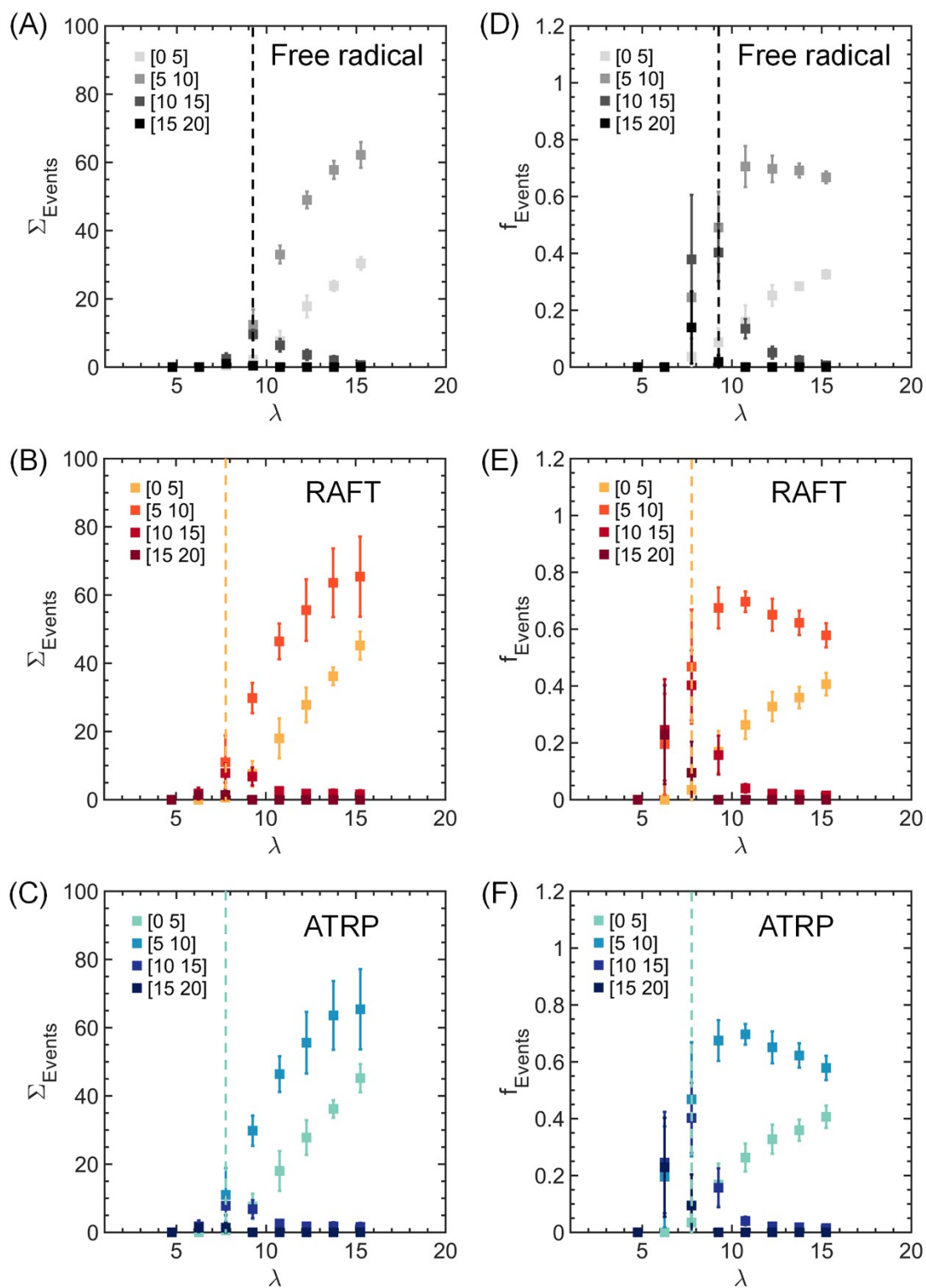


Figure S33. The count (a, c, e) and fraction (b, d, f) of the closest distances between chain scission events, for FRP (top panel), RAFT (middle panel) and ATRP (bottom panel).

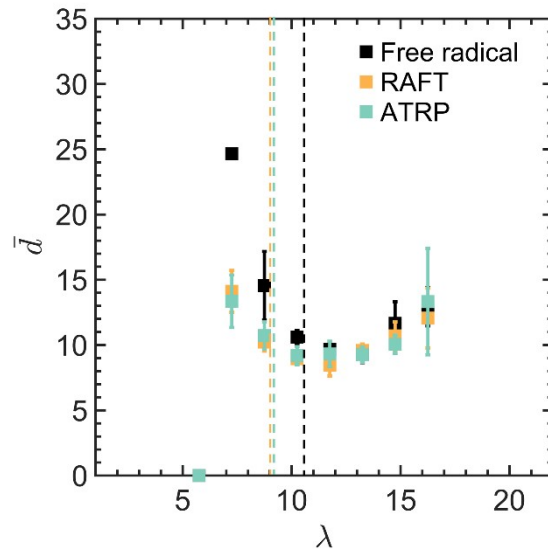


Figure S34. Average distance, \bar{d} , between scission events in polymer networks. This distance is much shorter in networks synthesized by RAFT and ATRP, indicating an earlier transition from random to correlated chain scission before fracture. Dashed lines represent the critical stretch for crack propagation.

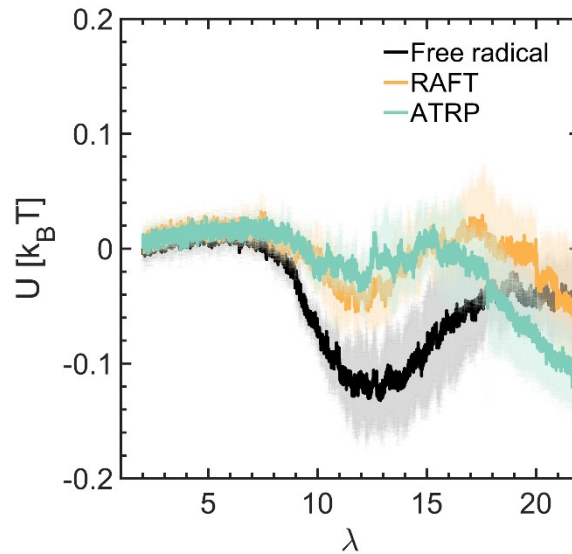


Figure S35. Potential energy in the networks during deformation. FRP-synthesized networks feature a lower potential energy at the failure point, indicating their more dissipative character compares to RAFT and ATRP-synthesized networks.

REFERENCES

1. Slooman, J., Yeh, C. J., Millereau, P., Comtet, J. & Creton, C. A molecular interpretation of the toughness of multiple network elastomers at high temperature. *Proc. Natl. Acad. Sci. U. S. A.* **119**, 1–11 (2022).
2. Dookhith, A. Z., Zhang, Z., Ganesan, V. & Sanoja, G. E. Impact of Reversible Deactivation Radical Copolymerizations (RDRPs) on Gelation, Phase Separation, and Mechanical Properties of Polymer Networks. *Macromolecules* (2024) doi:10.1021/acs.macromol.4c00905.
3. Furuya, T. & Koga, T. Molecular simulation of polymer gels synthesized by free radical copolymerization: Effects of concentrations and reaction rates on structure and mechanical properties. *Polymer (Guildf)*. **279**, 126012 (2023).
4. Furuya, T. & Koga, T. Comparison of gels synthesized by controlled radical copolymerization and free radical copolymerization: molecular dynamics simulation. *Soft Matter* **20**, 1164–1172 (2023).
5. Polanowski, P., Jeszka, J. K., Krysiak, K. & Matyjaszewski, K. Influence of intramolecular crosslinking on gelation in living copolymerization of monomer and divinyl cross-linker. Monte Carlo simulation studies. *Polymer (Guildf)*. **79**, 171–178 (2015).
6. Lyu, J. *et al.* Monte Carlo Simulations of Atom Transfer Radical (Homo)polymerization of Divinyl Monomers: Applicability of Flory-Stockmayer Theory. *Macromolecules* **51**, 6673–6681 (2018).
7. Case, L. C. Branching in polymers. I. Network defects. *J. Polym. Sci.* **45**, 397–404 (1960).
8. Scanlan, J. The effect of Network Flaws on the Elastic Properties of Vulcanizates. *J. Polym. Sci.* **43**, 501–508 (1960).
9. Zhang, Z. *et al.* Topology and Mechanical Properties of Polymer Networks Formed Under Free Radical and Atom Transfer Radical Polymerizations. *Macromolecules* 1–40 (2025) doi:10.1021/acs.macromol.4c03138.